

# Heterostructured WO<sub>3</sub>@CoWO<sub>4</sub> bilayer nanosheets for enhanced visible-light photo, electro and photoelectro-chemical oxidation of water

Huayang Zhang,<sup>a,1</sup> Wenjie Tian,<sup>a,1</sup> Yunguo Li,<sup>c,1</sup> Hongqi Sun,<sup>b,\*</sup> Moses O. Tadé,<sup>a</sup> and Shaobin Wang<sup>a,\*</sup>

Received 00th January 20xx,  
Accepted 00th January 20xx

DOI: 10.1039/x0xx00000x

www.rsc.org/

Herein, a facile interface-induced synthesis method is first established to newly fabricate two-dimensional (2D) bilayer nanosheets of WO<sub>3</sub>@CoWO<sub>4</sub> as highly efficient catalysts for enhanced photo, electro and photoelectro-chemical oxygen evolution reactions (OERs). The heterostructure and the interfacial oxygen vacancy of WO<sub>3</sub>@CoWO<sub>4</sub> reduce the energy barriers in OER. Density functional theory (DFT) calculations and material characterizations reveal that WO<sub>3</sub>@CoWO<sub>4</sub> p-n heterojunction endows the composite with a narrowed band gap for better visible-light harvesting, rapid charge transfer across the interface and a lower recombination rate of the photo-excited carriers. The interface O-vacancy vests the active Co site with an enhanced density of state (DOS) at valence band maximum (VBM), which can increase the concentration of the photogenerated holes to improve photocatalytic and photoelectrochemical (PEC) activity. This study presents a proof-of-concept design towards low cost and multi-metal 2D/2D nanosheets for water oxidation applications.

## 1. Introduction

As an emerging technology for solar energy conversion and storage, photocatalytic and photoelectrochemical (PEC) splitting of water into H<sub>2</sub> and O<sub>2</sub> has attracted tremendous attention for sustainable environment and energy development.<sup>1–3</sup> In this course, decomposition of water to dissociative oxygen (known as water oxidation or OER) is kinetically sluggish, due to the multi-step, four-electron and multi-proton transfer processes. Rational design of efficient photocatalytic or PEC water oxidation catalysts (WOCs) is essential for advancing the technologies toward efficient water-splitting into hydrogen.<sup>4,5</sup> Enormous efforts have been devoted to pursuing suitable semiconductor materials that can achieve efficient solar-energy-conversion and propel the complex water oxidation reactions by photo-generated holes.<sup>6,7</sup> Among them, low-cost tungsten oxide (WO<sub>3</sub>) has emerged as a promising n-type and visible-light-active semiconductor material, which possesses up to 12% solar spectrum absorption with a bandgap energy of 2.7 eV.<sup>8,9</sup> Nonetheless, the low photon energy conversion efficiency, instability caused by photo-corrosion, and poor kinetics of

pristine WO<sub>3</sub> usually result in an unsatisfactory activity in OER.<sup>10,11</sup>

It was revealed that WO<sub>3</sub> in a 2D nanosheet configuration has planar conduction channels, promoting the exposure of catalytically active facets to accelerate fast transport of the photoexcited charge carriers.<sup>12,13</sup> However, the long migration route in WO<sub>3</sub> makes it easy for electron-hole recombination. To solve this problem, construction of a heterojunction composite using two semiconductors is an excellent strategy.<sup>14,15</sup> As a p-type semiconductor with low cost and high stability, cobalt tungstate (CoWO<sub>4</sub>) has drawn our attention. We project that coupling WO<sub>3</sub> nanosheet with CoWO<sub>4</sub> nanosheet in a p-n heterostructure would be a promising WOC candidate. However, specific challenges have to be addressed in the synthesis of WO<sub>3</sub> nanosheet because it is a nonlayered compound and lacks the driving force for 2D anisotropic growth.<sup>16</sup> Therefore, the design and integration of CoWO<sub>4</sub>-WO<sub>3</sub> bilayered nanosheets are much more difficult. To the best of our knowledge, no such a material has been attempted and reported.

In this work, we elaborately propose a hydrothermal method to generate WO<sub>3</sub> nanosheets. Then, a scalable interface-induced strategy for bilayer formation was established by coating CoWO<sub>4</sub> onto WO<sub>3</sub> to obtain 2D WO<sub>3</sub>@CoWO<sub>4</sub> bilayer hybrids. In this format, CoWO<sub>4</sub> produces benefits to photocatalytic or PEC OER with triple functions: i) construction of WO<sub>3</sub>@CoWO<sub>4</sub> p-n heterojunction; ii) prevention of WO<sub>3</sub> from corrosion; iii) CoWO<sub>4</sub> as an active OER electrocatalyst<sup>17–19</sup> to serve as a cocatalyst to promote photocatalytic OER. For the first time,

<sup>a</sup> Department of Chemical Engineering, Curtin University, GPO Box U1987, WA 6845, Australia. \*E-mail: shaobin.wang@curtin.edu.au

<sup>b</sup> School of Engineering, Edith Cowan University, 270 Joondalup Drive, Joondalup, WA 6027, Australia. \*E-mail: h.sun@ecu.edu.au

<sup>c</sup> Department of Earth Sciences, University College London, Gower Street, London WC1E 6BT, United Kingdom.

<sup>1</sup> Authors contributed equally.

Electronic Supplementary Information (ESI) available: See DOI: 10.1039/x0xx00000x

evident enhancement of electrochemical, visible-light photocatalytic and PEC water oxidation performance was verified simultaneously. Moreover, we performed DFT calculations for structural insights to the enhanced electro/photochemical and PEC activities of WO<sub>3</sub>@CoWO<sub>4</sub> nanosheets.

## 2. Experimental section

### 2.1. Synthesis of WO<sub>3</sub> nanosheets.

WO<sub>3</sub> nanosheets were synthesized via a hydrothermal method. In detail, 0.38 g of tungstic acid was dispersed in 27 mL deionized (DI) water, followed by dissolving 0.5 g thiourea in the solution. The suspension was then transferred into a 50 mL Teflon liner and sealed in an autoclave. The autoclave was heated at 180 °C for 24 h. The precipitates were separated using a centrifuge and washed with DI water and ethanol for several times. Finally, WO<sub>3</sub> powders were obtained after drying at 60 °C.

### 2.2. Synthesis of WO<sub>3</sub>@CoWO<sub>4</sub> nanosheet composites.

The obtained WO<sub>3</sub> (0.1 g) was dispersed into 10 mL DI water under stirring for 10 min at room temperature. After that, certain amount of Co(NO<sub>3</sub>)<sub>2</sub>·6H<sub>2</sub>O was added into the suspension solution and stirred for another 10 min. Then, 2.5 mL ammonium hydroxide solution was added dropwise into the above solution and stirred for 1 h at room temperature before evaporating at 80 °C. Finally, the residual powders were collected and heated at 300 °C for 2 h under air with a heating rate of 5 °C min<sup>-1</sup>. The synthesized catalysts were designated as WO<sub>3</sub>@CoWO<sub>4</sub>-1, WO<sub>3</sub>@CoWO<sub>4</sub>-2, WO<sub>3</sub>@CoWO<sub>4</sub>-3, and WO<sub>3</sub>@CoWO<sub>4</sub>-4, and WO<sub>3</sub>@CoWO<sub>4</sub>-5 according to the different additive amount of Co(NO<sub>3</sub>)<sub>2</sub>·6H<sub>2</sub>O at 3.2 mg, 6.4 mg, 9.6 mg, 64 mg and 128 mg, respectively.

### 2.3. Electrochemical measurements.

Electrocatalytic tests were conducted in N<sub>2</sub>-saturated 0.1 M KOH in a three-electrode electrochemical system using a rotating disk electrode (RDE) configuration (Pine Instrument Company, USA), which is controlled by a Gamry electrochemical workstation (Reference 3000). Ag/AgCl (KCl sat.) and Pt wire were adopted as the reference electrode and the counter electrode, respectively.

Preparation of working electrode is described as follows: 7 mg catalyst was added into a solution containing 25 μL Nafion<sup>®</sup> 117 solution and 500 μL ethanol to generate a suspension by sonication. Then, 10 μL of the catalyst ink was dripped onto a glassy carbon electrode (5.0 mm in diameter) and dried in air. All potentials were converted into reversible hydrogen electrode (RHE) values based on equation (1):

$$E_{RHE} = E_{Ag/AgCl} + 0.059\text{pH} + 0.197\text{ V} \quad (1)$$

The electrodes were activated by running cyclic voltammetry (CV) cycles from 1.2 to 1.8 V (vs RHE) for at least 10 times till stable and reproducible curves were obtained. Then, polarization curves using linear sweep voltammetry (LSV) were recorded

with a rotation speed of 1600 rpm at a scan rate of 5 mV s<sup>-1</sup>. The overpotential ( $\eta$ ) was calculated according to the following formula:

$$\eta = E_{RHE} - 1.23\text{ V} \quad (2)$$

All polarization plots were recorded after iR-correction. The accelerated durability tests (ADT) for WO<sub>3</sub>@CoWO<sub>4</sub>-4 were conducted by measuring CV cycles in potentials from 1.164 to 1.764 V (vs RHE) at a scan rate of 200 mV s<sup>-1</sup>. LSV of ADT after 1000 and 10000 CV cycles were recorded. To probe changes in double-layer capacitance ( $C_{dl}$ ) during ADT, CV cycles were tested from 1.25-1.30 V at scan rates of 10, 20, 30, 40, and 60 mV s<sup>-1</sup> before and after 1000 and 10000 cycles. The corresponding capacitive current densities at 1.275 V were plotted as a function of scan rate. The slope of the fitted line equals twice the value of  $C_{dl}$  and represents electrochemically active surface area (EASA). The EASAs of the other samples were evaluated using the same method for comparison. Further, chronoamperometric response (i-t) of WO<sub>3</sub>@CoWO<sub>4</sub>-4 was estimated at 1.614 V (vs. RHE) in 0.1 M KOH at 1600 rpm.

### 2.4. Photocatalytic oxygen evolution reaction tests.

For each reaction, 50 mg catalyst was dispersed in 50 mL phosphate buffer solution and the pH value was adjusted to around 6.8, followed by adding 0.49 g Na<sub>2</sub>SO<sub>4</sub>, 0.18 g Na<sub>2</sub>S<sub>2</sub>O<sub>8</sub> and 0.03 g [Ru(bpy)<sub>3</sub>]Cl<sub>2</sub>·6H<sub>2</sub>O. After that, the solution was transferred to a sealed double jacketed reactor (800 mL) with a quartz window, which was connected to an on-line gas chromatograph (Agilent 490 Micro GC) with a thermal conductivity detector. To remove air in the reactor completely, N<sub>2</sub> was pumped in for at least 30 min. Then, the solution was stabilized in the dark for 10 min, which was probed as the baseline. The solution was irradiated via a 300 W Xe lamp (Newport) through a light filter ( $\lambda > 420$  nm) and aligned to 200 mW/cm<sup>2</sup> (2 suns) to start the reaction. The reaction temperature was maintained at 25 °C by a flow of cooling water, controlled by a thermostatic water bath.

### 2.5. Photoelectrochemical Measurement.

Photoelectrochemical tests were carried out on a Zennium workstation (Zahner, Germany) in a three-electrode framework, with Ag/AgCl electrode as the reference electrode and Pt plate (1.5×1.5 cm<sup>2</sup>) as the counter electrode. F-doped tin oxide (FTO) glasses were adopted as the photoanode substrate, which were cleaned before use under sonication by acetone, ethanol, and distilled water successively. Samples were loaded onto the FTO as below: 8 mg catalyst, 25 μL Nafion 117 solutions and 500 μL ethanol were mixed by ultrasonication and 40 μL of the resulted suspension was loaded onto the 1×1 cm<sup>2</sup> FTO each time via a spin coating method. The photoanodes were obtained by annealing the FTO glasses at 300 °C for 30 min under air atmosphere. The PEC properties were measured via the linear sweep voltammetry (LSV) method under irradiation of AM 1.5G simulated solar light (light intensity: 1 sun or 100 mW cm<sup>-2</sup>) from 0.6 to 1.8 V (vs RHE) at a sweep rate of 10 mV s<sup>-1</sup>.

Electrochemical impedance spectra (EIS) measurements were carried out under dark and irradiation, respectively, in a frequency range of 100 kHz to 100 mHz. Potentiostatic response was measured at 1.23 V (vs RHE) under irradiation for 1 h. The Na<sub>2</sub>SO<sub>4</sub> solution (0.5 M, pH 6.8) as the electrolyte was purged with N<sub>2</sub> for 30 min prior to the measurement. Mott-Schottky analysis was carried out at a frequency of 1 kHz.

The details of Materials Characterizations and DFT calculation methods are provided in Supporting Information.

### 3. Results and discussion

#### 3.1. Synthesis and structure analysis.

X-ray diffraction (XRD) patterns (Fig. 1) indicate that WO<sub>3</sub> nanosheets have a hexagonal crystalline structure (h-WO<sub>3</sub>, JCPDS # 33-1387). Different WO<sub>3</sub>/CoWO<sub>4</sub> molar ratios of 1:0.026, 1:0.055, 1:0.083, 1:1 and 0.023:1 were prepared from WO<sub>3</sub>@CoWO<sub>4</sub>-1, -2, -3, -4 to -5, respectively. Accordingly, the diffraction peaks of monoclinic CoWO<sub>4</sub> (JCPDC 15-0867) enhance gradually in the five samples with CoWO<sub>4</sub> being as the main phase in WO<sub>3</sub>@CoWO<sub>4</sub>-5.

Transmission electron microscopy (TEM) images in Fig. 2a and Fig. S1a reveal the nanosheet morphology of WO<sub>3</sub>. The high-resolution TEM (HRTEM) analysis indicates that (001) planes are exposed planes of WO<sub>3</sub> (Fig. 2b). WO<sub>3</sub>@CoWO<sub>4</sub> composites display very similar nanosheet morphologies (Fig. 2c and S1-S5). Fig. 2d (WO<sub>3</sub>@CoWO<sub>4</sub>-3) depicts the close atomic bonding between the (200) planes of CoWO<sub>4</sub> and the (001) planes of WO<sub>3</sub> with interface defects and vacancies caused by lattice mismatches. These defects or vacancies are also observed in

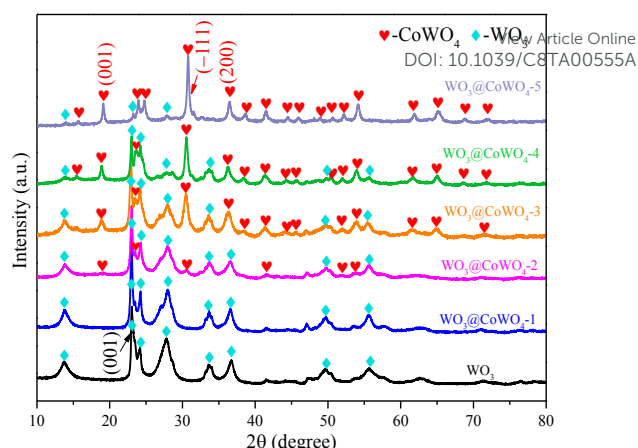


Fig. 1 XRD patterns of WO<sub>3</sub> and WO<sub>3</sub>@CoWO<sub>4</sub> composites.

other composites (Fig. S2-S5). The presence of O vacancies in the composites can also be verified by the signal of W<sup>5+</sup> ( $g = 1.96$ ) in the representative solid-state EPR test on WO<sub>3</sub>@CoWO<sub>4</sub>-3 (Fig. S6).<sup>20</sup>

Representative three-dimensional (3D) atomic force microscopy (AFM) measurements (Fig. 2e and f) on WO<sub>3</sub>@CoWO<sub>4</sub>-3 show that the nanosheets could be thinner than 10 nm. High angle annular dark field scanning TEM (HAADF-STEM) and corresponding energy-dispersive X-ray spectroscopy (EDX) elemental mapping images of the composites (Fig. 2g, S2c, S3c, S4c and S5c) implicates the different coverage levels of CoWO<sub>4</sub> on WO<sub>3</sub>. The full-scan X-ray photoelectron spectroscopy (XPS) spectra of WO<sub>3</sub> and WO<sub>3</sub>@CoWO<sub>4</sub>-3 are provided in Fig. S7. The peaks in W 4f spectra centering at 35.6, and 37.8 eV are ascribed to the spin-orbit splitting of W 4f<sub>7/2</sub> and W 4f<sub>5/2</sub>, illustrating W<sup>6+</sup> as the dominant valence state in both

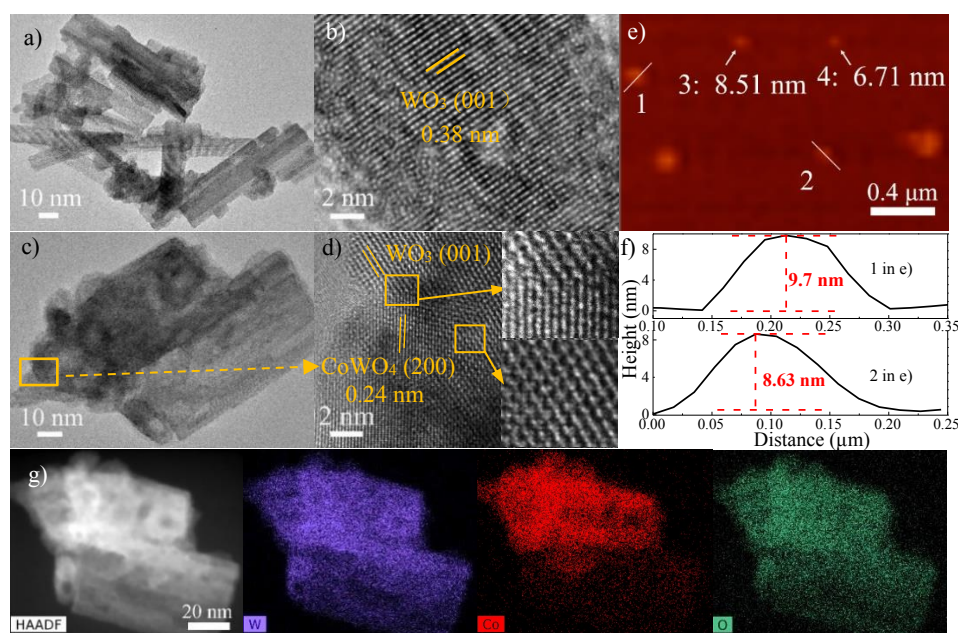


Fig. 2 TEM and HRTEM images of a, b) WO<sub>3</sub> and c, d) WO<sub>3</sub>@CoWO<sub>4</sub>-3. e) 3D AFM image of WO<sub>3</sub>@CoWO<sub>4</sub>-3 and f) thickness data of 1, 2 in e). g) HAADF-STEM image of WO<sub>3</sub>@CoWO<sub>4</sub>-3 and its EDX elemental mapping analysis.



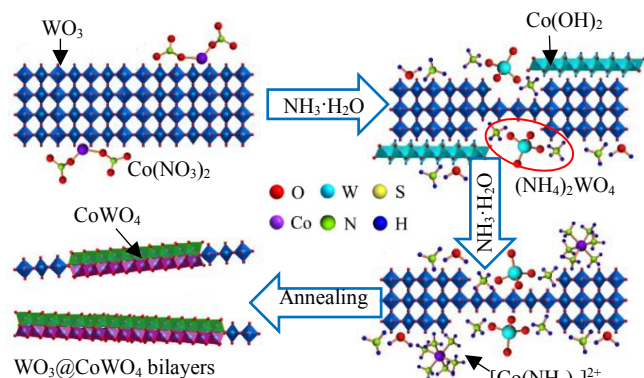


Fig. 3 Schematic showing of the formation process of WO<sub>3</sub>@CoWO<sub>4</sub> bilayer nanosheets.

samples.<sup>21,22</sup> In the O1s spectra (Fig. S7c), the peak at 530.4 eV can be associated with oxygen bonded to metal species, whereas the one centred at 531.6 eV is typical of the low coordination oxygen ions on the surface.<sup>23,24</sup> Co 2p spectrum featured the main peaks of Co 2p<sub>3/2</sub> at 781.4 and Co 2p<sub>1/2</sub> at 796.7 eV with separate satellite shake-up lines and spin energy separation of 15.3 eV, indicating the typical oxidation state of Co<sup>2+</sup> (Fig. S7d).<sup>22,23</sup>

The formation mechanism of the bilayer nanosheet composite is briefly proposed in Fig. 3. During the dropwise addition of NH<sub>3</sub>·H<sub>2</sub>O into a Co(NO<sub>3</sub>)<sub>2</sub> solution with dispersed WO<sub>3</sub>, Co(OH)<sub>2</sub> formed initially, but it was dissolved by excess NH<sub>3</sub>·H<sub>2</sub>O to generate a [Co(NH<sub>3</sub>)<sub>6</sub>]<sup>2+</sup> complex.<sup>25</sup> Meanwhile, partial WO<sub>3</sub> can be transformed into (NH<sub>4</sub>)<sub>2</sub>WO<sub>4</sub> by NH<sub>3</sub>·H<sub>2</sub>O,<sup>26</sup> which will interact with the [Co(NH<sub>3</sub>)<sub>6</sub>]<sup>2+</sup> to form [Co(NH<sub>3</sub>)<sub>6</sub>]WO<sub>4</sub> or CoWO<sub>4</sub> sediments on the surface of residual WO<sub>3</sub>. After annealing in air, stable WO<sub>3</sub>@CoWO<sub>4</sub> nanosheets were obtained. It is a simultaneous process of continuous WO<sub>3</sub> exfoliation and in-situ CoWO<sub>4</sub> coating, which results in thinner layers of WO<sub>3</sub> and CoWO<sub>4</sub> in the composites.

### 3.2. Characterization of the electrochemical OER performance.

The electrocatalytic OER activity of the samples was evaluated by polarization curves (Fig. 4a). The overpotential at a current density (J) of 10 mA cm<sup>-2</sup> is a criterion for assessing OER properties. WO<sub>3</sub> was almost inactive in the electrocatalytic OER. With higher CoWO<sub>4</sub> loading in the composites, the electrocatalytic activity increased dramatically and then declined. WO<sub>3</sub>@CoWO<sub>4</sub>-4 gave the smallest overpotential of 0.38 V, which is lower than commercial RuO<sub>2</sub> (0.40 V).

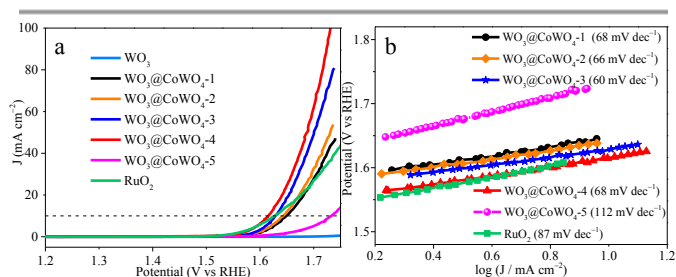


Fig. 4 a) Polarization curves tested in 0.1M KOH and b) the corresponding Tafel plots.

WO<sub>3</sub>@CoWO<sub>4</sub>-5 displayed an enlarged overpotential, attributable to fewer interface defects from low WO<sub>3</sub> content. These defects can serve as catalytically active sites in OER, proved by the DFT calculations shown later. The Tafel plots (Fig. 4b) indicated smaller Tafel slopes of WO<sub>3</sub>@CoWO<sub>4</sub>-1, -2, -3 and -4 than RuO<sub>2</sub>, suggesting their more favorable OER kinetics.<sup>27</sup> WO<sub>3</sub>@CoWO<sub>4</sub>-5 showed a much higher Tafel slope. As the best OER catalyst, WO<sub>3</sub>@CoWO<sub>4</sub>-4 displayed excellent durability, as provided in Fig. S8 and Supporting Information. In addition, WO<sub>3</sub>@CoWO<sub>4</sub> composites all displayed much higher electrochemically active surface area (EASA) than WO<sub>3</sub>, with WO<sub>3</sub>@CoWO<sub>4</sub>-4 to be the highest. (Fig. S9). This result indicates that abundant active sites were introduced to WO<sub>3</sub> by loading of CoWO<sub>4</sub>.

### 3.3. Visible-light photocatalytic OER performance.

Fig. 5a displays photocatalytic OER activities of the samples. Elevated performance was observed on WO<sub>3</sub>@CoWO<sub>4</sub> composites compared with WO<sub>3</sub>. With rising CoWO<sub>4</sub>/WO<sub>3</sub> ratios, the OER activity increased first and then decreased. WO<sub>3</sub>@CoWO<sub>4</sub>-3 presented the highest O<sub>2</sub> evolution rate (1.6 mmol g<sup>-1</sup> O<sub>2</sub> in 1 h), which is over 9 times higher than WO<sub>3</sub>. This rate is among the highest values reported for nonprecious metallic OER catalysts, as compared in Table S2.

A series of photo-dependent tests were carried out on the synthesized samples. As shown in UV-visible diffuse reflectance spectra (UV-Vis DRS, Fig. 5b), the visible light absorption intensity of the composites gradually improved with increasing CoWO<sub>4</sub> loadings. In addition, a red shift occurred in the absorption band-edge of the composites, reflecting better absorption at longer wavelengths. WO<sub>3</sub> presented a positive slope, typical for n-type semiconductors in the Mott-Schottky (M-S) plot (Fig. 5c). Since CoWO<sub>4</sub> is a p-type semiconductor with a negative slope, inverted “V-shapes” were then observed on WO<sub>3</sub>@CoWO<sub>4</sub> composites, reflecting a well-matched p-n heterostructure.<sup>28–30</sup> Fig. 5d shows a band structure diagram for WO<sub>3</sub>@CoWO<sub>4</sub> system. The conduction band minimum (CBM) of WO<sub>3</sub> (0.73 eV) was evaluated from the flat band potential of the M-S plot (Fig. 5c). The band gap of WO<sub>3</sub> (2.40 eV) was obtained from the Tauc’s plot (Fig. S10). VBM was acquired by the sum of CBM and band gap. Since we did not prepare pure CoWO<sub>4</sub>, the band structure data of CoWO<sub>4</sub> were obtained by DFT calculations using the monoclinic CoWO<sub>4</sub> slab (M-1, Fig. S11a). The band gap (2.84 eV), CBM (-0.11 eV) and VBM (2.73 eV) of CoWO<sub>4</sub> were obtained via the corresponding DOS (Fig. S11b), which are close to those values reported in the literature.<sup>31</sup> The band gap of the WO<sub>3</sub>@CoWO<sub>4</sub> system can be narrowed with CoWO<sub>4</sub> as the VBM, and WO<sub>3</sub> as the CBM, which helps explain their better light-harvesting ability than WO<sub>3</sub>. Since the CBM of CoWO<sub>4</sub> is more negative than WO<sub>3</sub>, it is thermodynamically favorable for the photo-excited electrons to move from CoWO<sub>4</sub> to WO<sub>3</sub>. Meanwhile, the holes generated in the valence bands of the two semiconductors can transfer from WO<sub>3</sub> to CoWO<sub>4</sub> due to their potential difference in VBM. Due to effective electron-hole separation by WO<sub>3</sub>@CoWO<sub>4</sub> heterojunction, their

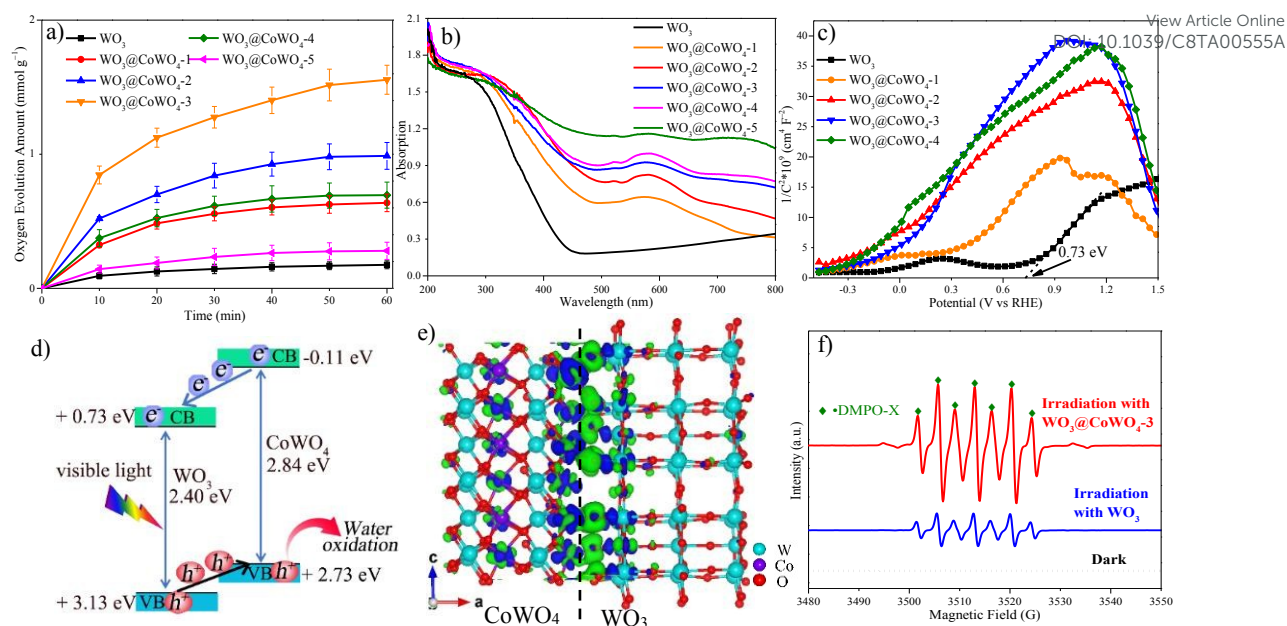


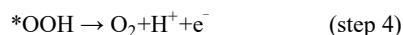
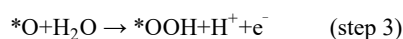
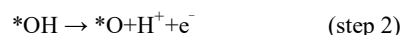
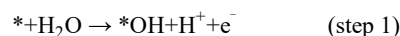
**Fig. 5** a) Visible-light photocatalytic OER activity. b) UV-Vis DRs and c) M-S plots. d) Band structure diagram (CB: Conduction band; VB: valence band; vs. NHE, pH=7). e) Charge density distribution for WO<sub>3</sub>@CoWO<sub>4</sub> (M-3): The green region indicates charge accumulation, while the blue area represents charge depletion; the isosurface value is 0.0038 e per Å<sup>3</sup>. f) Room temperature EPR signals tested in water oxidation system.

recombination rates would be largely reduced, inducing the enhanced photoactivity.<sup>32</sup> A large number of activated and migrated holes on the surface of CoWO<sub>4</sub> can efficiently oxidize the adsorbed H<sub>2</sub>O molecules into O<sub>2</sub>. Although WO<sub>3</sub>@CoWO<sub>4</sub>-4 exhibited the best electrochemical OER performance, its photocatalytic OER activity was much lower than WO<sub>3</sub>@CoWO<sub>4</sub>-3. It is conjectured that the excessive coverage of CoWO<sub>4</sub> on WO<sub>3</sub> in WO<sub>3</sub>@CoWO<sub>4</sub>-4 might block the photon absorption of WO<sub>3</sub>, which impairs the function of WO<sub>3</sub> in the heterostructure and leads to the deteriorated photocatalytic efficiency. As OER tends to occur at the side of CoWO<sub>4</sub> and WO<sub>3</sub> is physically coated by CoWO<sub>4</sub>, the corrosion of WO<sub>3</sub> by peroxy species generated during the OER process can be prevented. The stability of WO<sub>3</sub> can be improved.

To explore the charge redistribution across the WO<sub>3</sub>@CoWO<sub>4</sub> interface, molecular models including a hexagonal WO<sub>3</sub> slab (M-2) and a WO<sub>3</sub>@CoWO<sub>4</sub> slab (M-3) were constructed (as given in Fig. S12 and Supporting Information). The charge redistribution across the interface (Fig. 5e) was explored by subtracting the electronic charge of M-3 from those of the M-1 and M-2. Specifically, charge accumulation mainly occurs at the side of WO<sub>3</sub> while charge depletion focuses on CoWO<sub>4</sub> near the interface. Therefore, interface electric dipole forms at the interface, which enables electrons to transfer from CoWO<sub>4</sub> to WO<sub>3</sub> while the holes transfer from WO<sub>3</sub> to CoWO<sub>4</sub>.<sup>33</sup> This makes it easier for electron-hole transport and separation across the interface under light irradiation, which can also be experimentally demonstrated by photoluminescence (PL) spectra (Fig. S13). As shown, the lower luminescence intensity of the composites than WO<sub>3</sub> suggests the reduced charge recombination.

Room temperature in-situ electron paramagnetic resonance (EPR) was performed in this water oxidation system with 5, 5-dimethyl-1-pyrroline N-oxide (DMPO) as the trapping agent (Fig. 5f). No visible signal was obtained under dark. Interestingly, active seven-line paramagnetic signals were captured as 'DMPO-X' under irradiation after adding WO<sub>3</sub> or WO<sub>3</sub>@CoWO<sub>4</sub>-3, which might arise from the excessive oxidation of DMPO by peroxide generated during OER.<sup>34-36</sup>

In general, water oxidation reaction proceeds via four-electron-transfer steps based on the following mechanism:<sup>27</sup>



where \* denotes the surface site.

Peroxy species (\*OOH) serve as the intermediates in the third step and can be readily decomposed into O<sub>2</sub>. The system with

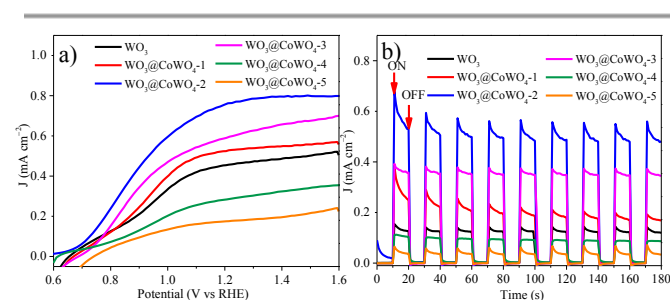


**Fig. 6** a) Current-voltage curves of the composites under illumination; b) i-t curves at a potential of 1.0 V (vs RHE) under light ON-OFF cycling.

## ARTICLE

Journal Name

WO<sub>3</sub>@CoWO<sub>4</sub>-3 displayed much stronger peak signals of DMPO-X than that with WO<sub>3</sub>, indicating the higher concentration of peroxy species and the more active OER performance.

### 3.4. Photoelectrochemical (PEC) OER performance.

Based on the enhanced electro and photo-catalytic OER performance of WO<sub>3</sub>@CoWO<sub>4</sub> composites, their PEC properties were further evaluated. Current-voltage curves were first recorded under dark (Fig. S14). By comparison, all the photoanodes presented deeply enhanced anodic photocurrent densities upon illumination (Fig. 6a). Compared to WO<sub>3</sub>, the photocurrent density of the composites firstly improved significantly along with the increased loading of CoWO<sub>4</sub> on WO<sub>3</sub> with WO<sub>3</sub>@CoWO<sub>4</sub>-2 reaching a maximum. The photocurrent density of WO<sub>3</sub>@CoWO<sub>4</sub>-2 is about 2 times larger than that of WO<sub>3</sub> at 1.3 V. However, the anodic photocurrent densities decreased dramatically in WO<sub>3</sub>@CoWO<sub>4</sub>-3, -4 and -5 with further higher ratios of CoWO<sub>4</sub>. Similar to the above discussion in photocatalytic OER test, this phenomenon can be explained by the destruction of the optimum synergistic function of heterostructure for PEC activity. The transient photoresponse of the composites were assessed by measuring i-t curves at 1.0 V (Fig. 6b). Prompt and steady photocurrent responses can be captured on the photoanodes during on and off cycles of illumination, which had the same trend with Fig. 6a. It is noted that an applied bias is imposed on the photoanode during PEC OER, which promotes the output of the photogenerated electrons in WO<sub>3</sub> through FTO-glass. The electron-hole recombination rate is reduced and thus the OER activity of WO<sub>3</sub> is largely elevated in PEC test compared with that in photocatalysis. Due to the different mechanisms, WO<sub>3</sub> exhibited the worst performance in photocatalysis but it was not the worst in PEC OER and the optimal CoWO<sub>4</sub>/WO<sub>3</sub> ratio was also various in the two systems.

EIS measurements were conducted on the photoanodes under dark and irradiation, respectively (Fig. S15). Compared to those collected under dark, all the semicircles in EIS were largely minished under irradiation, proving the lowered charge transfer resistance by photo-induced charge carries. Especially, WO<sub>3</sub>@CoWO<sub>4</sub>-2 exhibited the smallest resistance diameter, which helps explain its highest photocurrent response in PEC test. Therefore, an appropriate construction of WO<sub>3</sub>/CoWO<sub>4</sub> heterostructure could effectively boost the conductivity and PEC activity of WO<sub>3</sub>.

Besides, the instability of WO<sub>3</sub> caused by photo-corrosion was largely improved. As provided in Fig. S16, WO<sub>3</sub>@CoWO<sub>4</sub>-2 (decayed by 4 %) exhibited much better long-term PEC stability than WO<sub>3</sub> (decayed by 57 %) tested by the potentiostatic method.

### 3.5. DFT calculations for OER.

To study the effect of interface oxygen vacancies or defects (as verified by Fig. 2d, S3b, S4b and S5b) on OER, M-4 (Fig. 7a) was built by removing an interface O in M-3. We probed

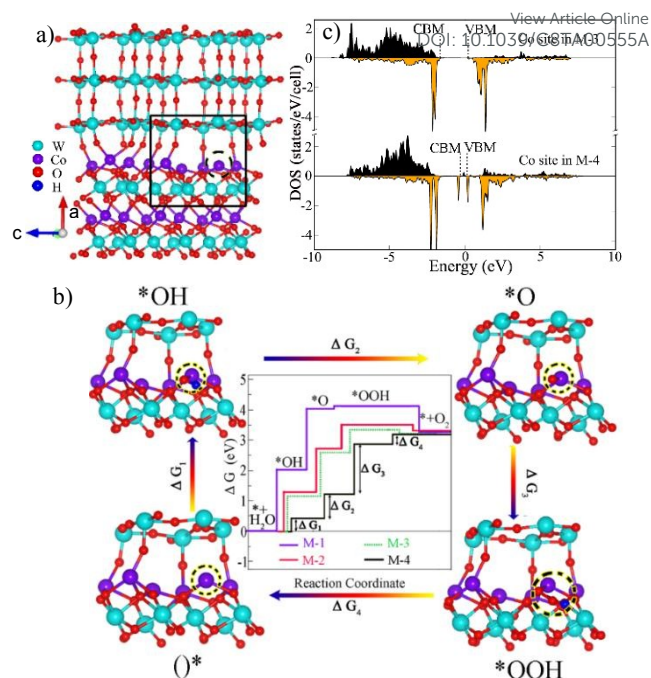


**Fig. 7** a) Molecular model of M-4; b) illustration of the Gibbs free energy changes for the four elementary steps of OER at pH = 7 and U = 0 in M-1, M-2, M-3 and M-4. Insets are close-up atomic structures of the selected area in M-4 which interpret the adsorption of intermediate species on active Co site. c) DOS of the selected Co site with and without O vacancy in M-3 and M-4.

adsorbates of \*OH, \*O and \*OOH on the surfaces terminated with Co (200) of CoWO<sub>4</sub> in M-1 (Fig. S17) and (001) surface planes of WO<sub>3</sub> in M-2 (Fig. S18). For M-3 and M-4, the adsorbates on the selected Co site of Co (200) interface were monitored, as provided in Fig. S19 and the inset images in Fig. 7b. This is because OER prefers to occur on the side of CoWO<sub>4</sub> in the composites due to migration of holes as analyzed in Fig. 5d and e. Moreover, Co sites are believed to be more active centres for OER in CoWO<sub>4</sub>.<sup>37,38</sup>

The specific Gibbs free energy changes during the four elementary steps are shown in Fig. 7b and Table S3. All adsorption scenarios in the four models shared uphill/endergonic energy profiles from \*OH (step 1), \*O (step 2) to \*OOH (step 3), suggesting that an external driving force (light irradiation or electrical potential) is required to initiate the OER reaction. Once the reaction got to \*OOH, the diagrams became downhill/exothermic in M-1, M-2 and M-3, indicating that step 4 is apt to happen and \*OOH will convert to O<sub>2</sub> (step 4) automatically. The step with the highest free energy barrier is referred as the overpotential-determining step.<sup>39</sup> It was noted that steps 1 and 2 were the potential-determining steps of WO<sub>3</sub>, while these energy barriers were lower in CoWO<sub>4</sub> with step 2 being the hardest one. CoWO<sub>4</sub> was catalytically more active than WO<sub>3</sub> in OER. Compared with CoWO<sub>4</sub>, the energy barriers in steps 1, 2 and 3 were reduced in M-3, indicating the lowered OER overpotential on WO<sub>3</sub>@CoWO<sub>4</sub> interface. This can be associated with the hole accumulation at the side of CoWO<sub>4</sub> across the interface (Fig. 5e). Interestingly, after an O was removed in the interface, the barriers in steps 1 and 2 were significantly lowered



(M-4), implying a simpler adsorption of water molecules onto the active Co site (step 1) and easier formation of OH\* (step 2). As these two initial steps were the hardest in M-1, M-2 and M-3, their easier proceedings promoted by interface-O-vacancy were considered to contribute considerably to the overall OER activity in WO<sub>3</sub>@CoWO<sub>4</sub> composites. Therefore, the WO<sub>3</sub>@CoWO<sub>4</sub> interface and especially interface-O-vacancies can serve as active sites for both electro, photo-catalytic and PEC oxidation of water.

DOS of the designated Co site in M-3 and M-4 were projected in Fig. 7c. Especially, the interface-O-vacancy induced dramatically increased DOS of Co site at both VBM and CBM, which can accelerate the transport of photon-generated carriers under light irradiation.<sup>16,40</sup> Faster diffusion kinetics, higher photoconversion efficiency and higher concentration of the photogenerated holes to react with H<sub>2</sub>O can be achieved. Thus, interface-O-vacancies can not only reduce OER energy barriers but also induce enhanced photo-responsive behavior.

#### 4. Conclusions

In summary, a versatile method was proposed for the synthesis of WO<sub>3</sub>@CoWO<sub>4</sub> bilayer nanosheets as excellent WOCs for enhanced visible-light-driven photo, electro-catalytic and PEC OER processes. Because of the theoretically reduced OER barriers by WO<sub>3</sub>@CoWO<sub>4</sub> interface and the interface-O-vacancies, WO<sub>3</sub>@CoWO<sub>4</sub> displayed a low overpotential of 0.38 V in 0.1 M KOH for electrocatalysis. The creation of p-n heterojunctions and interface-O-vacancies can increase the photo-energy conversion efficiency and the water oxidation ability, enabling WO<sub>3</sub>@CoWO<sub>4</sub>-3 to present over 9-time-higher O<sub>2</sub> evolution rate than WO<sub>3</sub>. A larger photocurrent with high stability was also observed in WO<sub>3</sub>@CoWO<sub>4</sub>-2 for PEC OER. The paradigm we presented in this work could provide a refreshing perspective for pursuing and designing more efficient low-dimensional photocatalytic, electrocatalytic and PEC OER catalysts.

#### Conflicts of interest

There are no conflicts to declare.

#### Acknowledgements

This work was supported by the Australian Research Council (DP150103026 and DP130101319). Y. Li acknowledges support from the NSFC (Grant No. 11674131). The authors acknowledge the help from the Centre for Microscopy, Characterization and Analysis (CMCA) of The University of Western Australia and the WA X-Ray Surface Analysis Facility of Curtin University funded by the Australian Research Council LIEF grant LE120100026 for material characterizations.

#### References

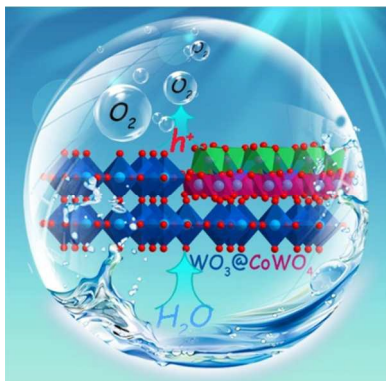
- S. Y. Reece, J. A. Hamel, S. Sung, T. D. Jarvi, A. J. Esswein, J. J. H. Pijpers and D. G. Nocera, *Science*, 2011, **334**, 645–648.
- T. Hisatomi, J. Kubota and K. Domen, *Chem. Soc. Rev.*, 2014, **43**, 7520–7535.
- X. Zong, H. Yan, G. Wu, G. Ma, F. Wen, L. Wang and C. Li, *J. Am. Chem. Soc.*, 2008, **130**, 7176–7177.
- T. Faunce, S. Styring, M. R. Wasielewski, G. W. Brudvig, A. W. Rutherford, J. Messinger, A. F. Lee, C. L. Hill, H. deGroot, M. Fontecave, D. R. MacFarlane, B. Hankamer, D. G. Nocera, D. M. Tiede, H. Dau, W. Hillier, L. Wang and R. Amal, *Energy Environ. Sci.*, 2013, **6**, 1074–1076.
- A. R. Parent, R. H. Crabtree and G. W. Brudvig, *Chem. Soc. Rev.*, 2013, **42**, 2247–2252.
- J. T. Kirner and R. G. Finke, *J. Mater. Chem. A*, 2017, **5**, 19560–19592.
- X. Li, J. Yu, J. Low, Y. Fang, J. Xiao and X. Chen, *J. Mater. Chem. A*, 2015, **3**, 2485–2534.
- N. Zhang, X. Li, H. Ye, S. Chen, H. Ju, D. Liu, Y. Lin, W. Ye, C. Wang, Q. Xu, J. Zhu, L. Song, J. Jiang and Y. Xiong, *J. Am. Chem. Soc.*, 2016, **138**, 8928–8935.
- J. Huang, Y. Zhang and Y. Ding, *ACS Catal.*, 2017, **7**, 1841–1845.
- A. Martínez-García, V. K. Vendra, S. Sunkara, P. Haldankar, J. Jasinski and M. K. Sunkara, *J. Mater. Chem. A*, 2013, **1**, 15235–15241.
- B. Zhang, X. L. Zheng, O. Voznyy, R. Comin, M. Bajdich, M. Garcia-Melchor, L. L. Han, J. X. Xu, M. Liu, L. R. Zheng, F. P. G. de Arquer, C. T. Dinh, F. J. Fan, M. J. Yuan, E. Yassitepe, N. Chen, T. Regier, P. F. Liu, Y. H. Li, P. De Luna, A. Janmohamed, H. L. L. Xin, H. G. Yang, A. Vojvodic and E. H. Sargent, *Science*, 2016, **352**, 333–337.
- J. Zhang, P. Zhang, T. Wang and J. Gong, *Nano Energy*, 2015, **11**, 189–195.
- J. Yan, T. Wang, G. Wu, W. Dai, N. Guan, L. Li and J. Gong, *Adv. Mater.*, 2015, **27**, 1580–1586.
- S. S. Kalanur, I.-H. Yoo, J. Park and H. Seo, *J. Mater. Chem. A*, 2017, **5**, 1455–1461.
- C. Yu, W. Zhou, L. Zhu, G. Li, K. Yang and R. Jin, *Appl. Catal. B Environ.*, 2016, **184**, 1–11.
- J.-S. Li, Y. Wang, C.-H. Liu, S.-L. Li, Y.-G. Wang, L.-Z. Dong, Z.-H. Dai, Y.-F. Li and Y.-Q. Lan, *Nat. Commun.*, 2016, **7**, 11204.
- T. Tian, J. Jiang and L. H. Ai, *Electrochim. Acta*, 2017, **224**, 551–560.
- H. Jia, J. Stark, L. Q. Zhou, C. Ling, T. Sekito and Z. Markin, *RSC Adv.*, 2012, **2**, 10874–10881.
- M. I. Ahmed, A. Adam, A. Khan, A. U. Rehman, M. Qamaruddin, M. N. Siddiqui and M. Qamar, *Mater. Lett.*, 2016, **183**, 281–284.
- Z. Lou, M. Zhu, X. Yang, Y. Zhang, M.-H. Whangbo, B. Li and B. Huang, *Appl. Catal. B Environ.*, 2018, **226**, 10–15.
- J. Zhang, Y. Ma, Y. Du, H. Jiang, D. Zhou and S. Dong, *Appl. Catal. B Environ.*, 2017, **209**, 253–264.
- J. F. Moulder, W. F. Stickle, P. E. Sobol and K. D. Bomben, *Phys. Electron. Inc.*, 1995, 261.
- S. Chen, G. Yang, Y. Jia and H. Zheng, *ChemElectroChem*,

- 2016, **3**, 1490–1496.
- 24 H. Zhang, W. Tian, L. Zhou, H. Sun, M. Tade and S. Wang, *Appl. Catal. B Environ.*, 2018, **223**, 2–9.
- 25 R. F. Sultan, *Phys. Chem. Chem. Phys.*, 2002, **4**, 1253–1261.
- 26 J. E. Yourey, J. B. Kurtz and B. M. Bartlett, *J. Phys. Chem. C*, 2012, **116**, 3200–3205.
- 27 H. Y. Wang, S. F. Hung, H. Y. Chen, T. S. Chan, H. M. Chen and B. Liu, *J. Am. Chem. Soc.*, 2016, **138**, 36–39.
- 28 J. Ke, J. Liu, H. Sun, H. Zhang, X. Duan, P. Liang, X. Li, M. O. Tade, S. Liu and S. Wang, *Appl. Catal. B Environ.*, 2017, **200**, 47–55.
- 29 Z. Liu, J. Tian, D. Zeng, C. Yu, L. Zhu, W. Huang, K. Yang and D. Li, *Mater. Res. Bull.*, 2017, **94**, 298–306.
- 30 X. Yan, Z. Wu, C. Huang, K. Liu and W. Shi, *Ceram. Int.*, 2017, **43**, 5388–5395.
- 31 T. Montini, V. Gombac, A. Hameed, L. Felisari, G. Adami and P. Fornasiero, *Chem. Phys. Lett.*, 2010, **498**, 113–119.
- 32 C. Yu, G. Li, S. Kumar, K. Yang and R. Jin, *Adv. Mater.*, 2014, **26**, 892–898.
- 33 W. Fan, C. Li, H. Bai, Y. Zhao, B. Luo, Y. Li, Y. Ge, W. Shi and H. Li, *J. Mater. Chem. A*, 2017, **5**, 4894–4903.
- 34 R. G. Li, Y. X. Weng, X. Zhou, X. L. Wang, Y. Mi, R. F. Chong, H. X. Han and C. Li, *Energy Environ. Sci.*, 2015, **8**, 2377–2382.
- 35 J. Tian, Z. Wu, Z. Liu, C. Yu, K. Yang, L. Zhu, W. Huang and Y. Zhou, *Chinese J. Catal.*, 2017, **38**, 1899–1908.
- 36 H. Zhang, W. Tian, X. Guo, L. Zhou, H. Sun, M. O. Tade and S. Wang, *ACS Appl. Mater. Interfaces*, 2016, **8**, 35203–35212.
- 37 J. Suntivich, K. J. May, H. a Gasteiger, J. B. Goodenough and Y. Shao-horn, *Science*, 2011, **334**, 2010–2012.
- 38 C. Ling, L. Q. Zhou and H. Jia, *RSC Adv.*, 2014, **4**, 24692–24697.
- 39 B. T. Zhao, L. Zhang, D. X. Zhen, S. Yoo, Y. Ding, D. C. Chen, Y. Chen, Q. B. Zhang, B. Doyle, X. H. Xiong and M. L. Liu, *Nat. Commun.*, **8**, 14586.
- 40 F. C. Lei, Y. F. Sun, K. T. Liu, S. Gao, L. Liang, B. C. Pan and Y. Xie, *J. Am. Chem. Soc.*, 2014, **136**, 6826–6829.

View Article Online  
DOI: 10.1039/C8TA00555A



## Graphical abstracts



Novel  $\text{WO}_3@CoWO_4$  bilayer nanosheets exhibit largely enhanced water oxidation performances compared with  $\text{WO}_3$  in electrocatalysis, visible-light photocatalysis and photoelectrochemistry.